Supporting Information

From rust to riches: phytochemically assisted doping of superparamagnetic Fe_3O_4 nanoparticles with Au for SERS sensing

Dariush Aligholizadeh[1,2], Landon Bechdel[1], Mansoor Johnson[1], Vera Smolyaninova[3], and Mary Sajini Devadas[1*]

1. Department of Chemistry, Towson University, Towson, Maryland 21252, USA
2. University of Maryland Baltimore-County, Baltimore, Maryland 21250, USA
3. Department of Physics, Astronomy, and Geosciences, Towson University, Towson, Maryland 21252, USA

∗ Corresponding author e-mail: mdevadas@towson.edu

Table of Contents

Table S1. Anthocynanin values for four independent trials on the *C. Canadensis* extract demonstrating an average anthocyanin concentration of 105 ± 16 μM. 5

Fig. S1. UV-vis absorption spectrum of the synthesized Au nanoparticle synthesized with *C. Canadensis* demonstrating a broad plasmon resonance centered around 540 nm. 6

Fig. S2. ATR-IR spectrum of citrate-capped Fe_3O_4 used as a template for Au loading. Six main bands are seen: (1) 535 cm^{-1} from Fe-O, (2) 1048^{-1} from C-O-C of the citrate ligand, (3) 1071 cm^{-1} from C-O-C of the citrate ligand, (4) 1389 cm^{-1} from Fe-COO^-, (5) 1589 cm^{-1} from Fe-COO^-, (6) 3304 cm^{-1} from O-H of the citrate. 7

Table S2. Compiled theoretical assignments for Fe_3O_4 IR-active vibrational modes 8

Fig. S3. Annotated IR spectra for cysAuFe_3O_4 (left, yellow trace) and cysteamine powder (right, gray trace). Different simulated data (black trace) are seen due to the lack of protonation of the cysteamine in powdered form and the presence of an extra proton when dissolved in aqueous media. The lack of a 2075 cm^{-1} band (due to S-H stretching) in the cysAuMNP demonstrates the presence of an Au-S bond between the cysteamine and the Au nanoparticle. The simulated data for cysAuFe_3O_4 was obtained from the protonated form of cysteamine ($HS(CH_2)_2NH_3^+$) while the simulated data for the cysteamine powder was obtained from the neutral species ($HS(CH_2)_2NH_2$). The annotated peaks are described in Table S3. 9

Table S3. Vibrational assignments for cysteamine present in cysAuFe_3O_4 and cysteamine powder. Cys$Au Fe_3O_4$ was simulated using a protonated, or basic, form of cysteamine, and the powder was simulated using the neutral species. Theoretical frequencies are chosen such that the vibrational

modes of both are the same and are the closest wavenumber occurrence of each vibration to the protonated value. For example, if both a 691 cm^{-1} and 800 cm^{-1} ν(C-S) exist for the neutral species, the 691 cm^{-1} is shown in the table as it is closer to 710 cm^{-1} than 800 cm^{-1} is. 10

Fig. S4. Annotated IR spectra for tio$AuFe_3O_4$ (green trace) and tiopronin powder (gray trace) as well as the theoretical simulated spectra (black trace). Eight distinguishable peaks are found in the tio$AuFe_3O_4$ with four being attributable to Fe_3O_4 and the other four being attributable to the tiopronin powder. The lack of the 2528 cm^{-1} band due to thiol stretching indicates the presence of an Au-S in place of the S-H. The annotated peaks are described in Table S4. 11

Table S4. Vibrational assignments for the tiopronin present in tio$AuFe_3O_4$ and cysteamine powder. Tio$AuFe_3O_4$ and tiopronin powder were simulated using the neutral tiopronin species. 12

Fig. S5. Annotated IR spectra for his$AuFe_3O_4$ (dark blue trace) and tiopronin powder (gray trace) as well as the theoretical simulated spectra (black trace). Eight distinguishable peaks are found in the his$AuFe_3O_4$ with five being attributable to Fe_3O_4 and the other three being attributable to the tiopronin powder. The annotated peaks are described in Table S5. 13

Table S5. Vibrational assignments for the histidine present in his$AuFe_3O_4$ and histidine powder. The his$AuFe_3O_4$ and histidine powder were simulated using the neutral histidine species. 14

Fig. S6. Annotated IR spectra for glu$AuFe_3O_4$ (light blue trace) and tiopronin powder (gray trace) as well as the theoretical simulated spectra (black trace). Fourteen distinguishable peaks are found in the glu$AuFe_3O_4$ with four being attributable to Fe_3O_4 and the other ten being attributable to the tiopronin powder. The absence of the 2521 cm^{-1} band (S-H stretching) in the gluAuMNP demonstrates the presence of an Au-S bond between the glutathione and the Au. The annotated peaks are described in Table S6. 15

Table S6. Vibrational assignments for the glutathione present in glu$AuFe_3O_4$ and glutathione powder. Glu$AuFe_3O_4$ and glutathione powder were simulated using the neutral glutathione species. 16

Fig. S7. Raman spectra of the full window (1900-400 cm^{-1}) for all analytes annotated. (a) The overlay of all Raman spectra with the laser background (simply passing the laser through an empty vial), all clearly visible peaks are annotated. (b) The same overlay as (a), but the laser background is now subtracted from all samples and all clearly visible peaks are annotated. 17

Fig. S8. Magnetic saturation as a function of temperature for all nanoparticles synthesized over the range of 50-300 K. (a) bare Fe_3O_4, (b) gluAuMNP, (c) tioAuMNP, (d) cysAuMNP, and (e) AuMNP. All nanoparticles demonstrate the same shape of decline with cysAuMNP and gluAuMNP having the lowest magnetic saturation overall but still maintaining relatively high saturation as opposed to diamagnetic product (0 emu/g)..... 18

Fig. S9. Langevin functions fitted to experimental data from magnetic hysteresis (MH) for nanoparticle at 300 K. All black scatter-plot data corresponds to the MH loop measurements from the vibrating sample magnetometer for each nanoparticle. Colored Langevin function fits correspond to: (a) red for Fe_3O_4, (b) light blue for gluAuFe_3O_4, (c) green for tioAuFe_3O_4, (d) dark blue for hisAuFe_3O_4, and (e) yellow for cysAuFe_3O_4. Each Langevin fit was calculated using the standard equation $y = C * \coth z - 1z$, where $z = xs$. The values for *s* and *C* were found through parameter estimation, with the overall agreement between the Langevin function and the experimental data indicating the presence of superparamagnetism in the sample. Reduced χ^2 values are shown on the plot to indicate agreement between the fit and the experimental data, with values <1 indicating a good fit. 19

Fig. S10. Additional STEM images of the bare Fe_3O_4 nanoparticles in bright-field imaging mode. All samples (a-d) were taken with a 30 kV accelerating voltage and 13 pA current. All scale bar insets correspond to 100 nm in length. 20

Fig. S11. Additional STEM images for the tioAuFe_3O_4 nanoparticles. Images (a-c) were taken in bright-field imaging mode and (d) was taken in high-angle annular diffraction (HAADF) mode. All samples were imaged with 30 kV accelerating voltage and 13 pA current. 21

Fig. S12. Additional STEM images for the hisAuFe_3O_4 nanoparticles synthesized. All images (a-d) were taken in bright-field mode with an accelerating voltage of 30 kV and a current of 13 pA. 22

Fig. S13. Additional STEM images for the cysAuFe_3O_4 nanoparticles. All images (a-d) were taken in bright field mode with an accelerating voltage of 30 kV. Images (a) and (d) were taken with a current of 50 pA, while images (b) and (c) were taken with a current of 13 pA. 23

Fig. S14. Additional STEM images for the gluAuFe_3O_4 product synthesized. All images (a-d) were taken in bright field imaging mode with an accelerating voltage of 30 kV and a current of 13 pA. 24

Fig. S15. Additional Raman and SERS spectra of *p*-NTP with and without the nanoparticles synthesized. (a) Full range (1700-400 cm^{-1}) Raman and SERS spectrum of the analyte on its own (50 µM *p*-NTP) and then with the nanoparticles in solution. (b) Region of interest over the fingerprint peak (~1567 cm^{-1}) demonstrating the SERS enhancement when hisAuMNP, cysAuMNP, and AuNP are applied to the natural Raman signal of 50 µM *p*-NTP. 25

Fig. S16. Region of interest Raman/SERS spectrum over the 1080-1120 cm^{-1} band demonstrating the presence of a single peak in the dark red 50 µM *p*-NTP spectrum as opposed to splitting peaks in cysAuMNP, hisAuMNP, and the AuNP, as well as the tioAuMNP to some extent. The splitting phenomenon demonstrates the presence of a thiol-Au bond between the *p*-NTP and the Au nanoparticles. 26

Fig. S17. Calibration curves for the Raman and SERS measurements on the portable Raman spectrometer. The limit of detection (LOD) was calculated using the 3σ method. The LOD for the natural Raman signal of the *p*-NTP (a) was 566.5 µM at the most intense peak (1577 cm^{-1}). The SERS LOD for *p*-NTP (b) when using cysAuMNP (nanoparticle with highest EF) was 5.42 µM, roughly 100x lower than the Raman LOD. The linear dynamic range (c) for this measurement is shown to be in the region of roughly 20-50 µM with qualitative detection still achievable above this region. All measurements were completed in triplicate. 27

Section 1. Calculation of SERS enhancement factor. 28

Section 2. Optimized geometries and computational settings used for all four ligands. 31

Trial	Aqueous Extract	
	Mass of flowers (g)	**[Anthocyanin] (mM)**
1	1.000	0.105
2	1.000	0.121
3	1.000	0.0826
4	1.000	0.110
Average ± std. dev.	1.000	0.105 ± 0.016

Table S1. Anthocynanin values for four independent trials on the *C. Canadensis* extract demonstrating an average anthocyanin concentration of 105 ± 16 μM.

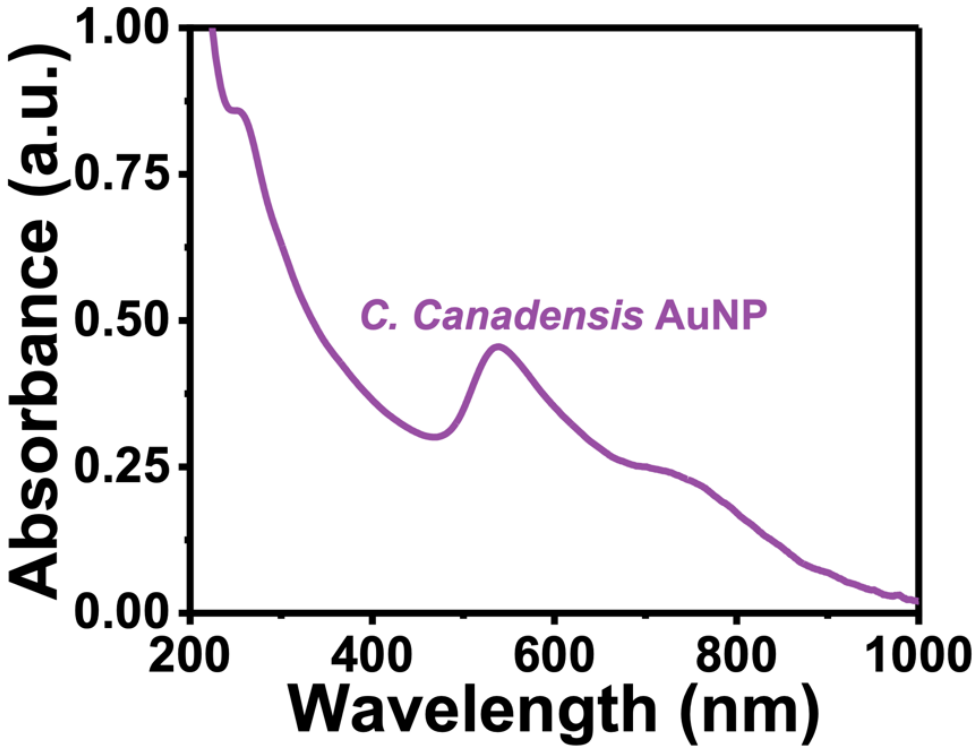

Fig. S1. UV-vis absorption spectrum of the synthesized Au nanoparticle synthesized with *C. Canadensis* demonstrating a broad plasmon resonance centered around 540 nm.

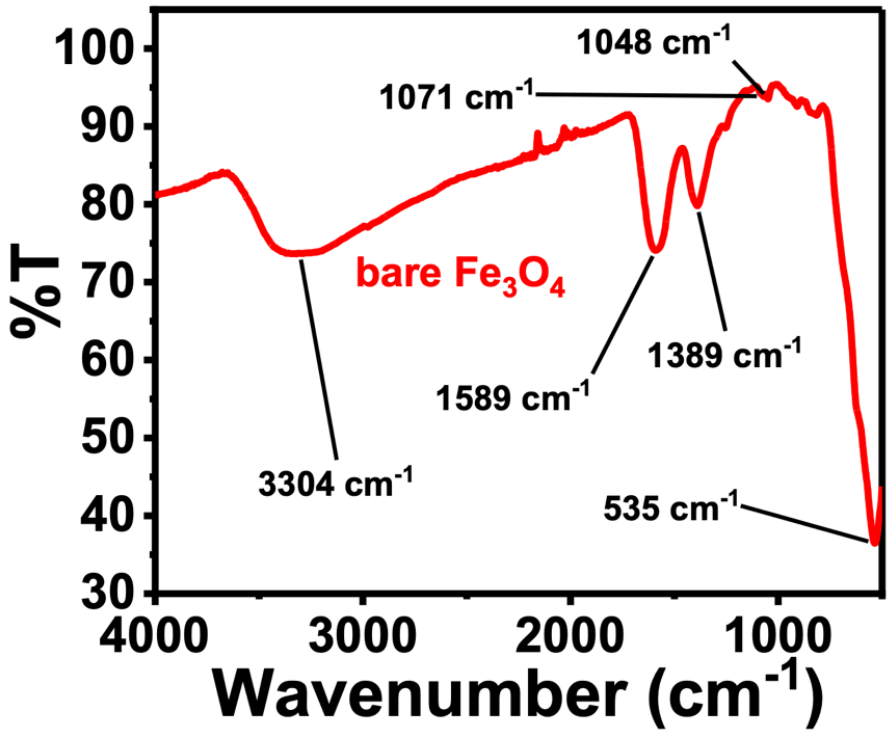

Fig. S2. ATR-IR spectrum of citrate-capped Fe_3O_4 used as a template for Au loading. Six main bands are seen: (1) 535 cm^{-1} from Fe-O, (2) 1048^{-1} from C-O-C of the citrate ligand, (3) 1071 cm^{-1} from C-O-C of the citrate ligand, (4) 1389 cm^{-1} from Fe-COO^-, (5) 1589 cm^{-1} from Fe-COO^-, (6) 3304 cm^{-1} from O-H of the citrate.

Table S2. Compiled theoretical assignments for Fe_3O_4 IR-active vibrational modes

Exp. Freq. (Fe_3O_4)	Theoretical Frequency [1, 2]	Vibrational Mode
535 cm^{-1}	578 cm^{-1}	ν(Fe-O)
1048 cm^{-1}	1020 cm^{-1}	δ(C-O-C)*
1071 cm^{-1}	1020 cm^{-1}	δ(C-O-C)*
1389 cm^{-1}	1428 cm^{-1}	ν(Fe-COO^-)*
1589 cm^{-1}	1521 cm^{-1}	ν(Fe-COO^-)*
3304 cm^{-1}	3126 cm^{-1}	ν(O-H)*

*: in part or totally contributed to by the citrate ligand, ν: stretching mode, δ: scissoring mode

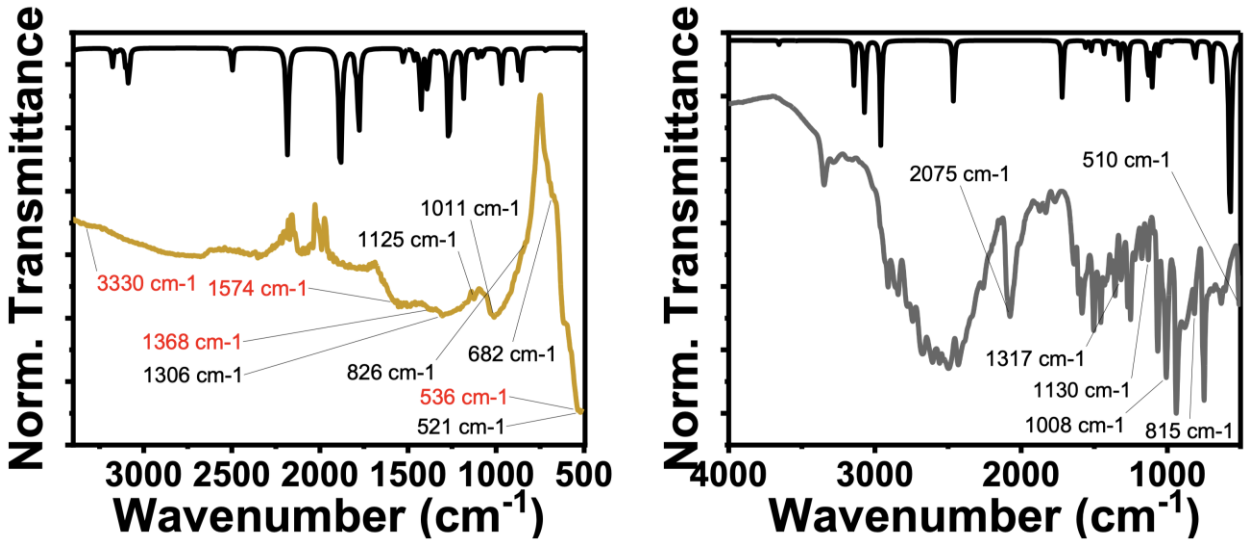

Fig. S3. Annotated IR spectra for cysAuFe_3O_4 (left, yellow trace) and cysteamine powder (right, gray trace). Different simulated data (black trace) are seen due to the lack of protonation of the cysteamine in powdered form and the presence of an extra proton when dissolved in aqueous media. The lack of a 2075 cm^{-1} band (due to S-H stretching) in the cysAuMNP demonstrates the presence of an Au-S bond between the cysteamine and the Au nanoparticle. The simulated data for cysAuFe_3O_4 was obtained from the protonated form of cysteamine ($HS(CH_2)_2NH_3^+$) while the simulated data for the cysteamine powder was obtained from the neutral species ($HS(CH_2)_2NH_2$). The annotated peaks are described in **Table S3**.

Table S3. Vibrational assignments for cysteamine present in cysAuFe_3O_4 and cysteamine powder. CysAuFe_3O_4 was simulated using a protonated, or basic, form of cysteamine, and the powder was simulated using the neutral species. Theoretical frequencies are chosen such that the vibrational modes of both are the same and are the closest wavenumber occurrence of each vibration to the protonated value. For example, if both a 691 cm^{-1} and 800 cm^{-1} ν(C-S) exist for the neutral species, the 691 cm^{-1} is shown in the table as it is closer to 710 cm^{-1} than 800 cm^{-1} is.

Exp. Freq. (cysAuMNP)	Exp. Freq. (Powder)	Theoretical Frequency (basic/neutral)	Vibrational Mode
521 cm^{-1}	510 cm^{-1}	519 cm^{-1}/–	τ(C-N)
536 cm^{-1}	–	–	ν(Fe-O)*
682 cm^{-1}	–	710 cm^{-1} / 691 cm^{-1}	ν(C-S)
826 cm^{-1}	815 cm^{-1}	849 cm^{-1} / 966 cm^{-1}	ν(C-C)
1011 cm^{-1}	1008 cm^{-1}	1071 cm^{-1} / 1052 cm^{-1}	ν(C-C)
1125 cm^{-1}	1130 cm^{-1}	1179 cm^{-1} / 1359 cm^{-1}	ρ(C-H)
1306 cm^{-1}	1317 cm^{-1}	1383 cm^{-1} / 1428 cm^{-1}	ω(C-H)
–	2075 cm^{-1}	2494 cm^{-1} / 2459 cm^{-1}	ν(S-H)#
1368 cm^{-1}	–	–	ν(Fe-COO^-)*
1574 cm^{-1}	–	–	ν(Fe-COO^-)*
3330 cm^{-1}	–	–	ν(O-H)*

#: thiol bonding mode, *: contributed to be the citrate-Fe_3O_4 core, ν: stretching mode, δ: scissoring mode, τ: on-axis rotational mode, ρ: rocking mode, ω: wagging mode

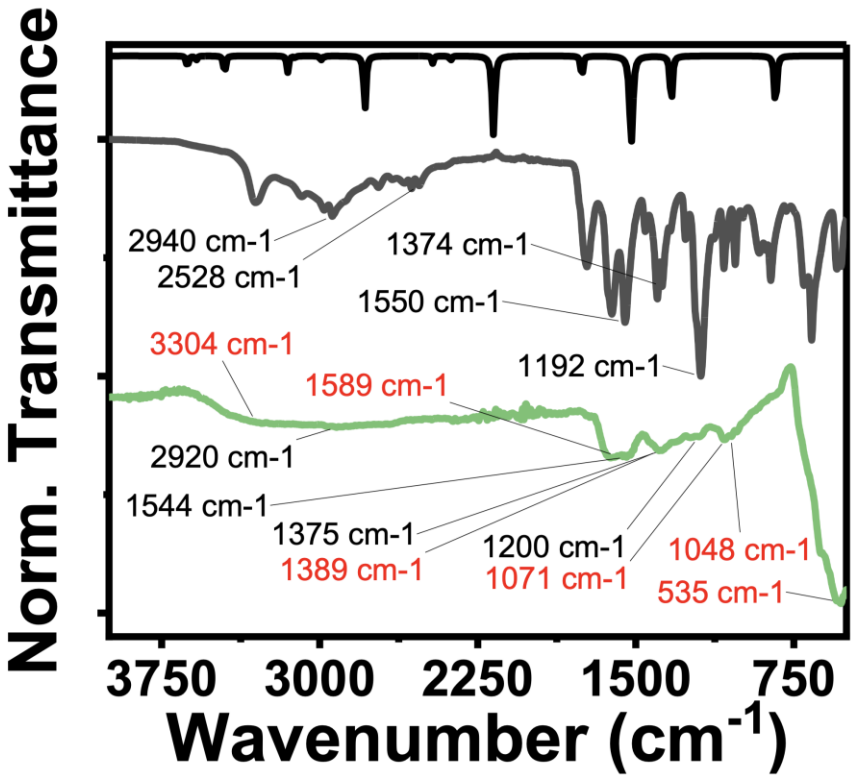

Fig. S4. Annotated IR spectra for tioAuFe_3O_4 (green trace) and tiopronin powder (gray trace) as well as the theoretical simulated spectra (black trace). Eight distinguishable peaks are found in the tioAuFe_3O_4 with four being attributable to Fe_3O_4 and the other four being attributable to the tiopronin powder. The lack of the 2528 cm^{-1} band due to thiol stretching indicates the presence of an Au-S in place of the S-H. The annotated peaks are described in **Table S4**.

Table S4. Vibrational assignments for the tiopronin present in tioAuFe_3O_4 and cysteamine powder. TioAuFe_3O_4 and tiopronin powder were simulated using the neutral tiopronin species.

Exp. Freq. (tioAuMNP)	Exp. Freq. (Powder)	Theoretical Frequency	Vibrational Mode
535 cm^{-1}	–	–	ν(Fe-O)*
1048 cm^{-1}	–	–	ν(C-O)*
1071 cm^{-1}	–	–	ν(C-O)*
1200 cm^{-1}	1192 cm^{-1}	1326 cm^{-1}	ν(N-H)
1375 cm^{-1}	1374 cm^{-1}	1516 cm^{-1}	ν(N-H), δ(C-N-C)
1389 cm^{-1}	–	–	ν(Fe-COO^-)*
1544 cm^{-1}	1550 cm^{-1}	1523 cm^{-1}	ν(C-S)
1589 cm^{-1}	–	–	ν(Fe-COO^-)*
–	2528 cm^{-1}	2461 cm^{-1}	ν(S-H)#
2920 cm^{-1}	2940 cm^{-1}	2977 cm^{-1}	ν(C-H)
3304 cm^{-1}	–	–	ν(O-H)*

#: thiol bonding mode, *: contributed to be the citrate-Fe_3O_4 core, ν: stretching mode

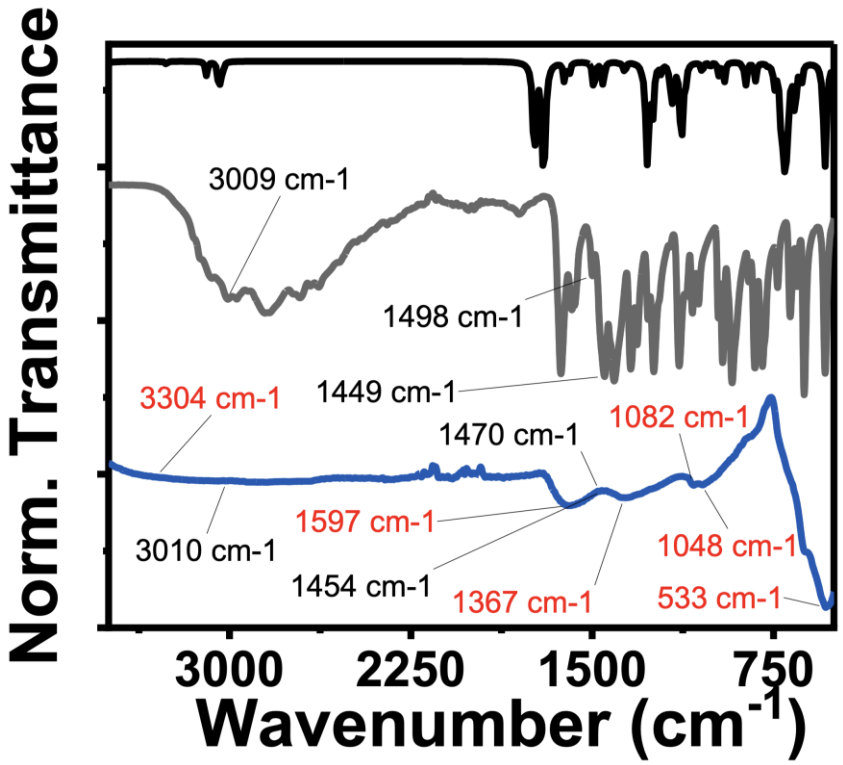

Fig. S5. Annotated IR spectra for hisAuFe_3O_4 (dark blue trace) and tiopronin powder (gray trace) as well as the theoretical simulated spectra (black trace). Eight distinguishable peaks are found in the hisAuFe_3O_4 with five being attributable to Fe_3O_4 and the other three being attributable to the tiopronin powder. The annotated peaks are described in **Table S5**.

Table S5. Vibrational assignments for the histidine present in hisAuFe_3O_4 and histidine powder. The hisAuFe_3O_4 and histidine powder were simulated using the neutral histidine species.

Exp. Freq. (hisAuMNP)	Exp. Freq. (Powder)	Theoretical Frequency	Vibrational Mode
533 cm^{-1}	–	–	ν(Fe-O)*
1048 cm^{-1}	–	–	ν(C-O)
1082 cm^{-1}	–	–	ν(C-O)
1367 cm^{-1}	–	–	ν(Fe-COO^-)*
1454 cm^{-1}	1449 cm^{-1}	1449 cm^{-1}	imidazole ring deformation
1470 cm^{-1}	1498 cm^{-1}	1488 cm^{-1}	imidazole ring deformation
1597 cm^{-1}	–	–	ν(Fe-COO^-)*
3010 cm^{-1}	3009 cm^{-1}	3042 cm^{-1}	ν(C-H)
3304 cm^{-1}	–	–	ν(O-H)*

*: contributed to be the citrate-Fe_3O_4 core, ν: stretching mode

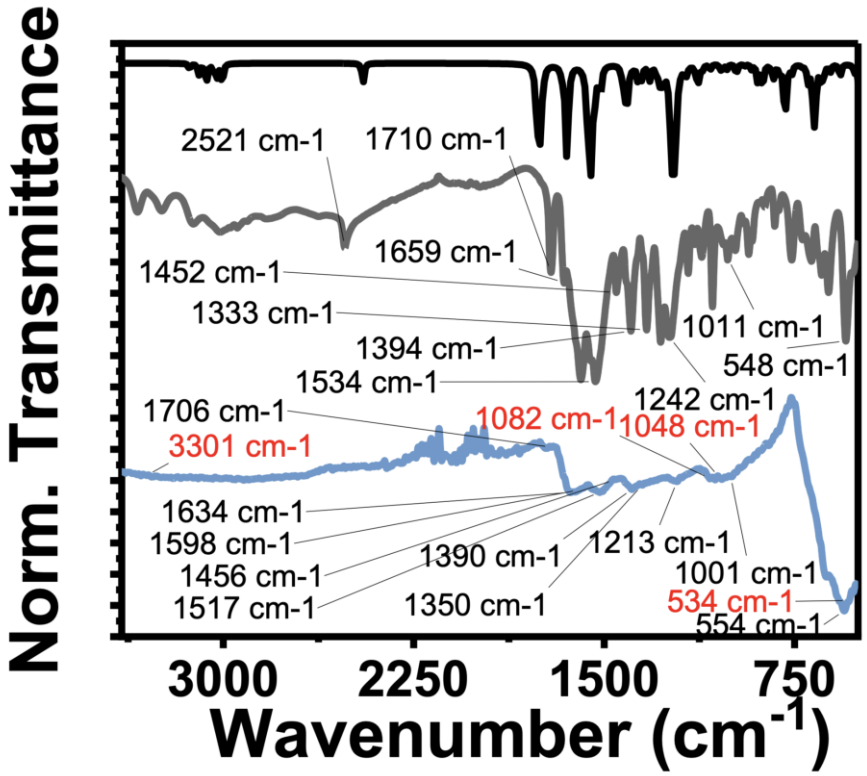

Fig. S6. Annotated IR spectra for gluAuFe_3O_4 (light blue trace) and tiopronin powder (gray trace) as well as the theoretical simulated spectra (black trace). Fourteen distinguishable peaks are found in the gluAuFe_3O_4 with four being attributable to Fe_3O_4 and the other ten being attributable to the tiopronin powder. The absence of the 2521 cm^{-1} band (S-H stretching) in the gluAuMNP demonstrates the presence of an Au-S bond between the glutathione and the Au. The annotated peaks are described in **Table S6**.

Table S6. Vibrational assignments for the glutathione present in gluAuFe_3O_4 and glutathione powder. Glu$AuFe_3O_4$ and glutathione powder were simulated using the neutral glutathione species.

Exp. Freq. (gluAuMNP)	Exp. Freq. (Powder)	Theoretical Frequency	Vibrational Mode
533 cm^{-1}	–	–	ν(Fe-O)*
554 cm^{-1}	548 cm^{-1}	484 cm^{-1}	ω(O-H)
1001 cm^{-1}	1011 cm^{-1}	1011 cm^{-1}	ν(C-C)
1048 cm^{-1}	–	–	ν(C-O)
1082 cm^{-1}	–	–	ν(C-O)
1213 cm^{-1}	1242 cm^{-1}	1225 cm^{-1}	ν(C-O)
1350 cm^{-1}	1333 cm^{-1}	1347 cm^{-1}	ω(C-H)
1390 cm^{-1}	1394 cm^{-1}	1407 cm^{-1}	δ(C-N-C)
1456 cm^{-1}	1452 cm^{-1}	1509 cm^{-1}	δ(H-C-H)
1517 cm^{-1}	1534 cm^{-1}	1548 cm^{-1}	ν(C-N)
1598 cm^{-1}	–	–	ν(Fe-COO^-)*
1634 cm^{-1}	1659 cm^{-1}	1642 cm^{-1}	ν(C=O)
1706 cm^{-1}	1710 cm^{-1}	1750 cm^{-1}	ν(C=O)
–	2521 cm^{-1}	2446 cm^{-1}	ν(S-H)#
3301 cm^{-1}	–	–	ν(O-H)*

#: thiol bonding mode, *: contributed to be the citrate-Fe3O4 core, ν: stretching mode, δ: scissoring mode, τ: on-axis rotational mode, ρ: rocking mode, ω: wagging mode

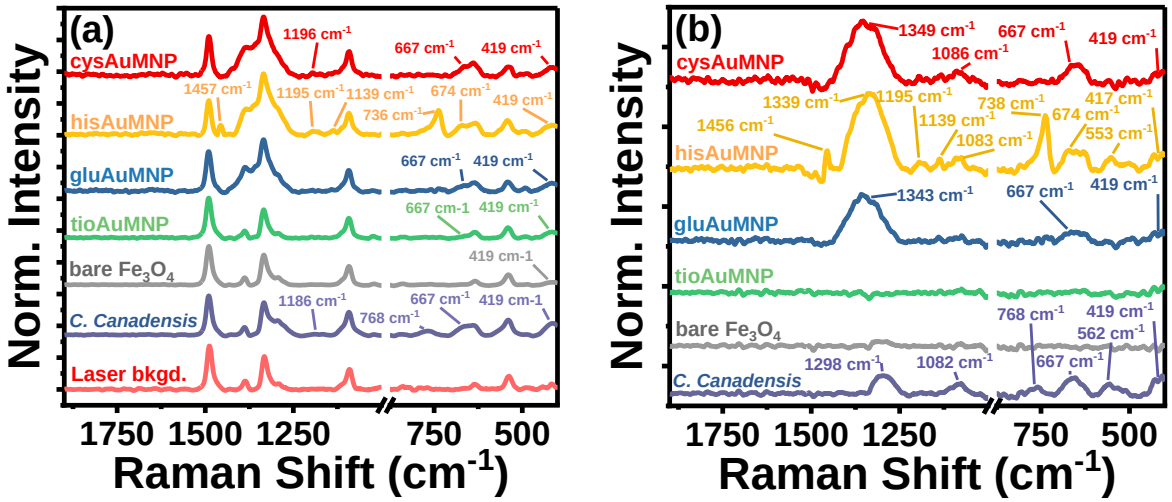

Fig. S7. Raman spectra of the full window (1900-400 cm^{-1}) for all analytes annotated. (a) The overlay of all Raman spectra with the laser background (simply passing the laser through an empty vial), all clearly visible peaks are annotated. (b) The same overlay as (a), but the laser background is now subtracted from all samples and all clearly visible peaks are annotated.

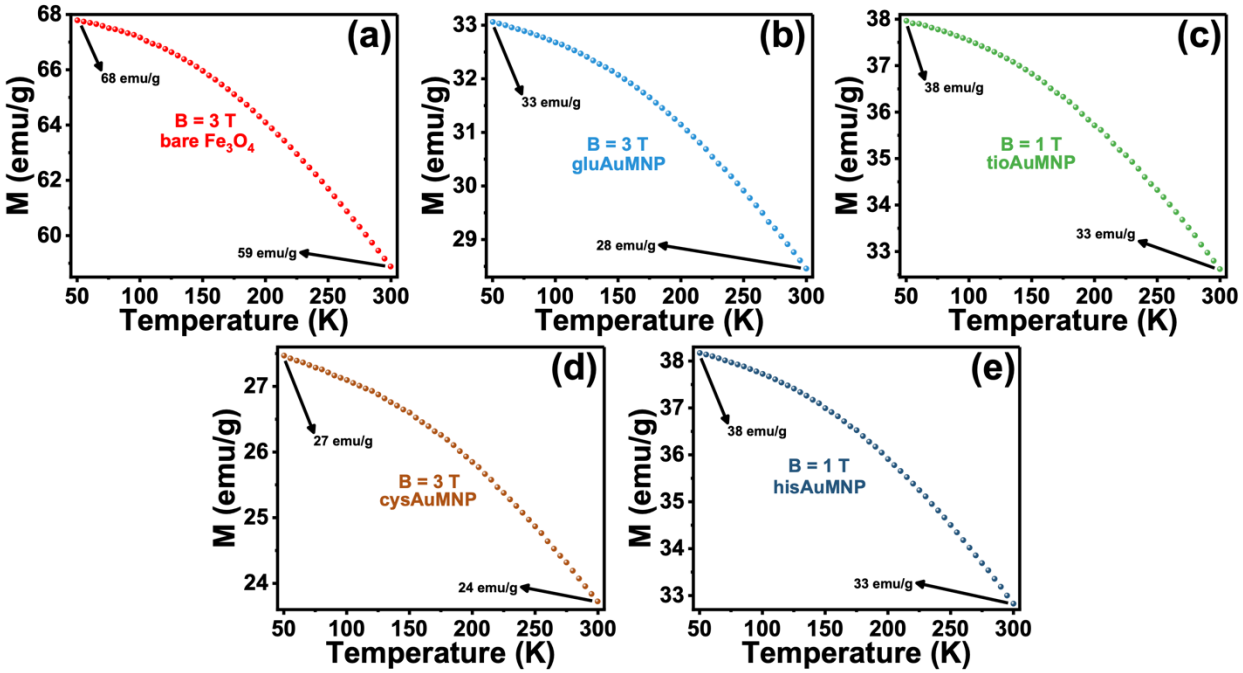

Fig. S8. Magnetic saturation as a function of temperature for all nanoparticles synthesized over the range of 50-300 K. (a) bare Fe_3O_4, (b) gluAuMNP, (c) tioAuMNP, (d) cysAuMNP, and (e) AuMNP. All nanoparticles demonstrate the same shape of decline with cysAuMNP and gluAuMNP having the lowest magnetic saturation overall but still maintaining relatively high saturation as opposed to diamagnetic product (0 emu/g).

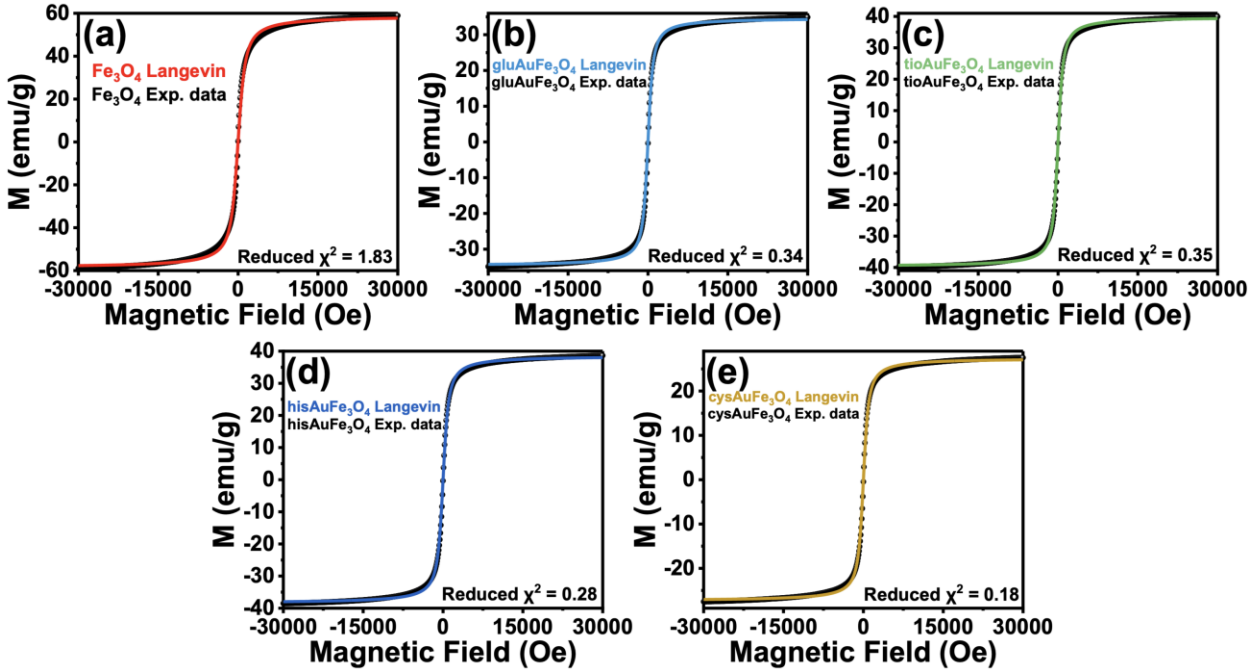

Fig. S9. Langevin functions fitted to experimental data from magnetic hysteresis (MH) for nanoparticle at 300 K. All black scatter-plot data corresponds to the MH loop measurements from the vibrating sample magnetometer for each nanoparticle. Colored Langevin function fits correspond to: (a) red for Fe_3O_4, (b) light blue for $gluAuFe_3O_4$, (c) green for $tioAuFe_3O_4$, (d) dark blue for $hisAuFe_3O_4$, and (e) yellow for $cysAuFe_3O_4$. Each Langevin fit was calculated using the standard equation $\boldsymbol{y = C * \left(\coth(z) - \frac{1}{z}\right)}$, where $\boldsymbol{z = \frac{x}{s}}$. The values for *s* and *C* were found through parameter estimation, with the overall agreement between the Langevin function and the experimental data indicating the presence of superparamagnetism in the sample. Reduced χ^2 values are shown on the plot to indicate agreement between the fit and the experimental data, with values <1 indicating a good fit.

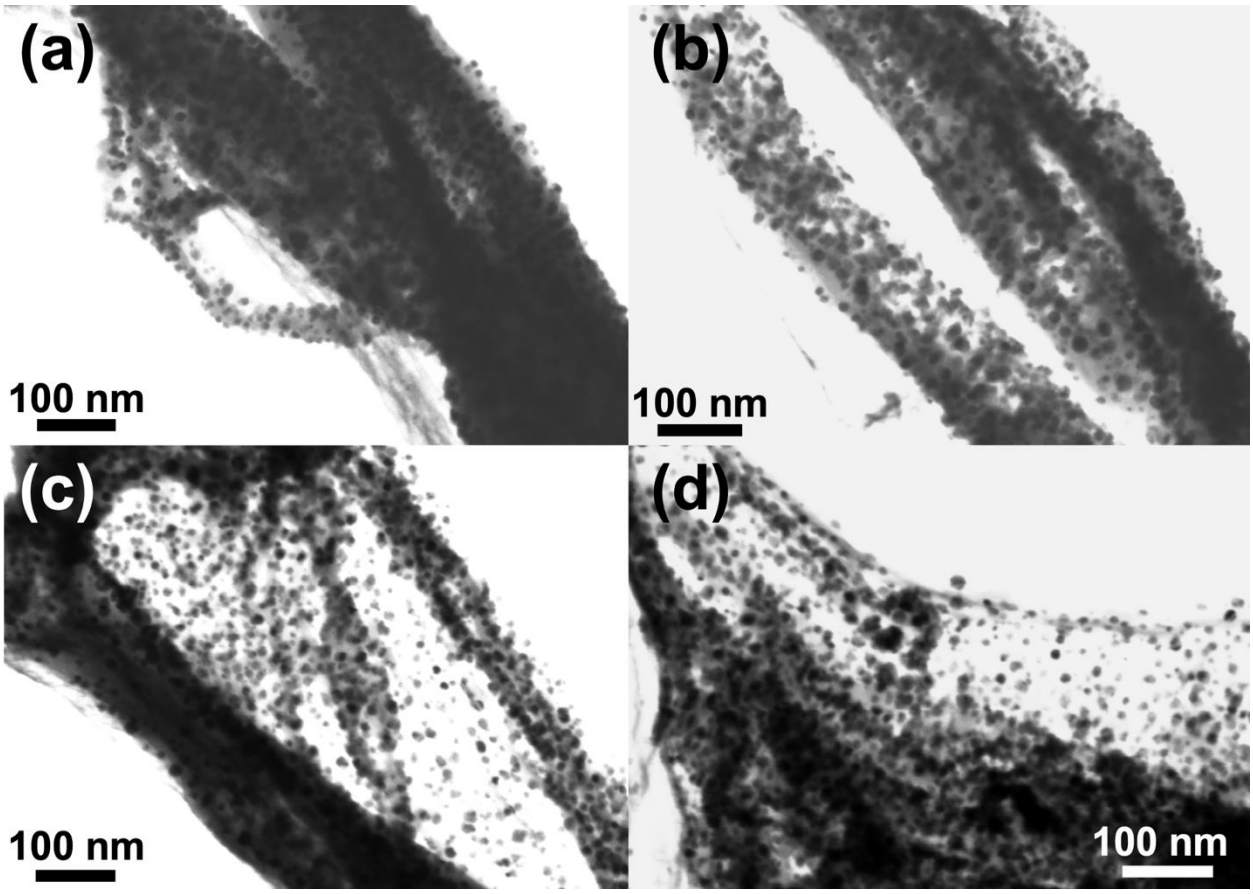

Fig. S10. Additional STEM images of the bare Fe_3O_4 nanoparticles in bright-field imaging mode. All samples (a-d) were taken with a 30 kV accelerating voltage and 13 pA current. All scale bar insets correspond to 100 nm in length.

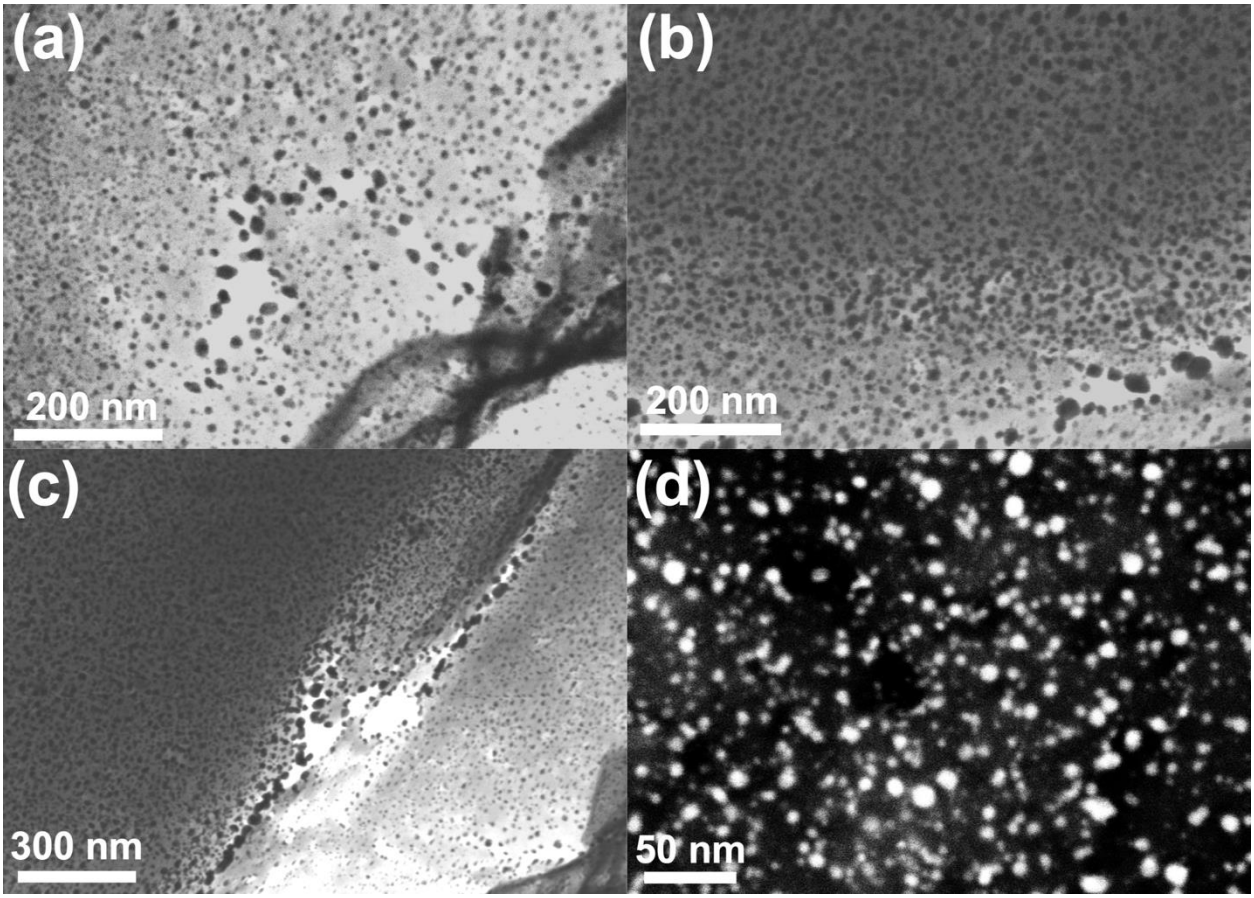

Fig. S11. Additional STEM images for the tio$AuFe_3O_4$ nanoparticles. Images (a-c) were taken in bright-field imaging mode and (d) was taken in high-angle annular diffraction (HAADF) mode. All samples were imaged with 30 kV accelerating voltage and 13 pA current.

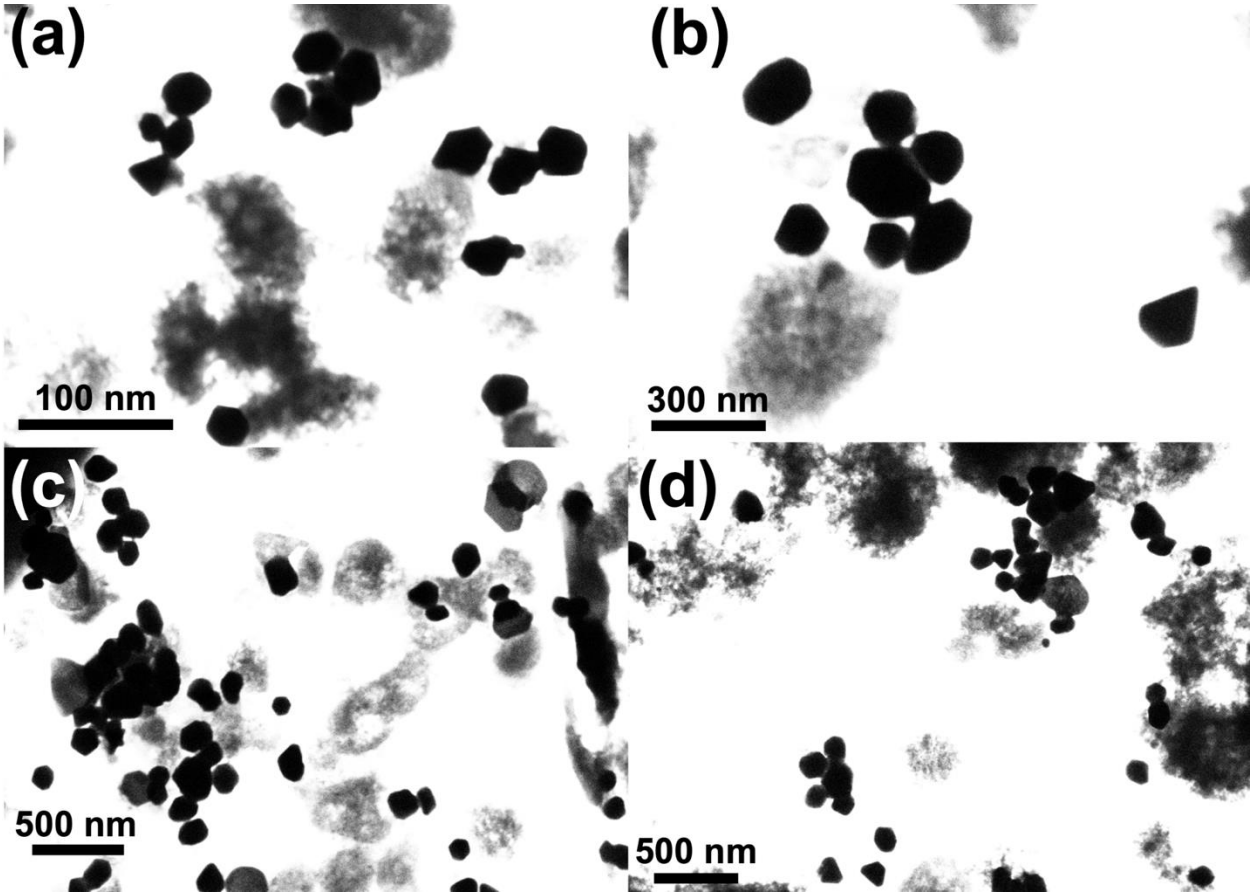

Fig. S12. Additional STEM images for the his$AuFe_3O_4$ nanoparticles synthesized. All images (a-d) were taken in bright-field mode with an accelerating voltage of 30 kV and a current of 13 pA.

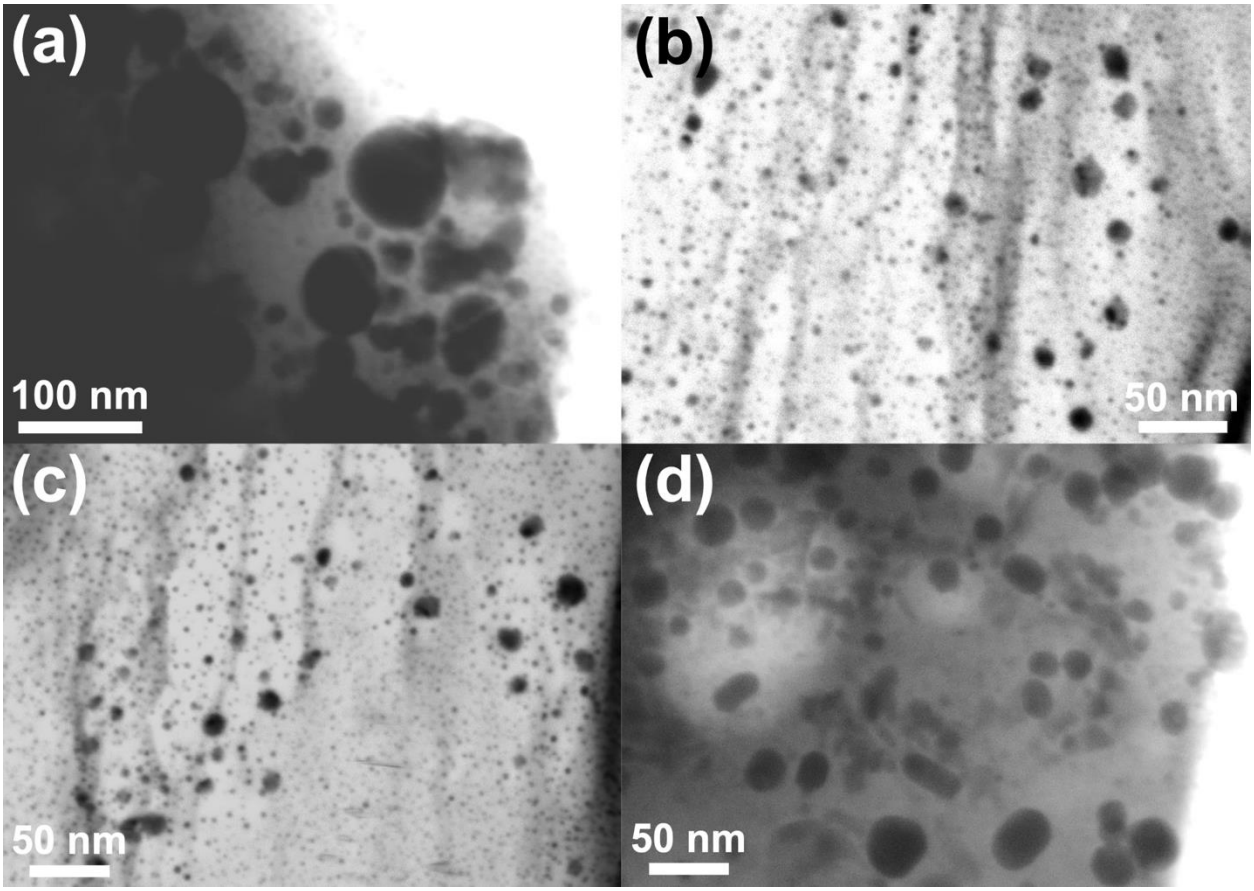

Fig. S13. Additional STEM images for the cysAuFe_3O_4 nanoparticles. All images (a-d) were taken in bright field mode with an accelerating voltage of 30 kV. Images (a) and (d) were taken with a current of 50 pA, while images (b) and (c) were taken with a current of 13 pA.

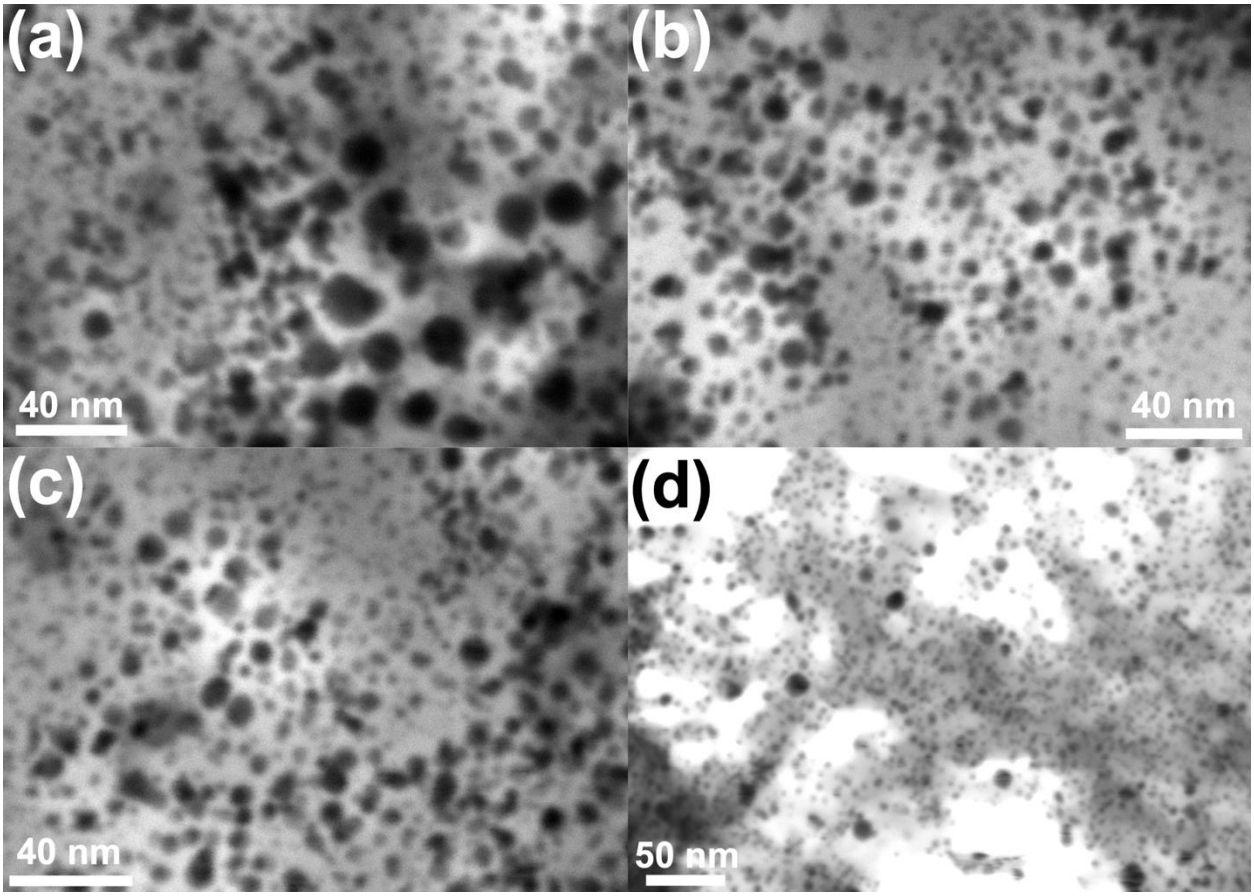

Fig. S14. Additional STEM images for the gluAuFe_3O_4 product synthesized. All images (a-d) were taken in bright field imaging mode with an accelerating voltage of 30 kV and a current of 13 pA.

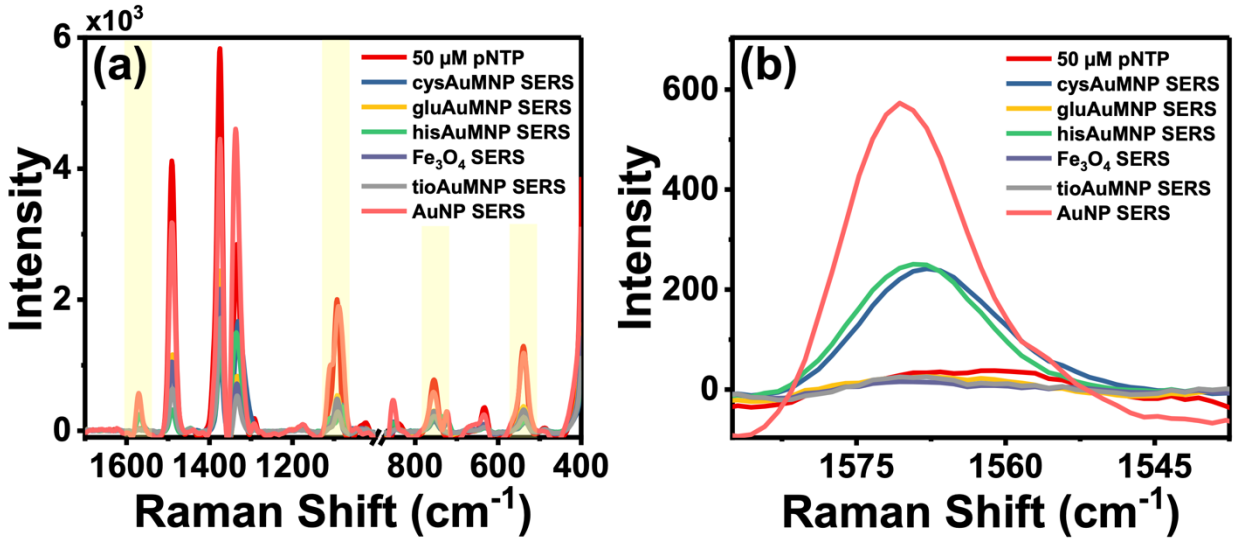

Fig. S15. Additional Raman and SERS spectra of *p*-NTP with and without the nanoparticles synthesized. (a) Full range (1700-400 cm^{-1}) Raman and SERS spectrum of the analyte on its own (50 µM *p*-NTP) and then with the nanoparticles in solution. (b) Region of interest over the fingerprint peak (~1567 cm^{-1}) demonstrating the SERS enhancement when hisAuMNP, cysAuMNP, and AuNP are applied to the natural Raman signal of 50 µM *p*-NTP.

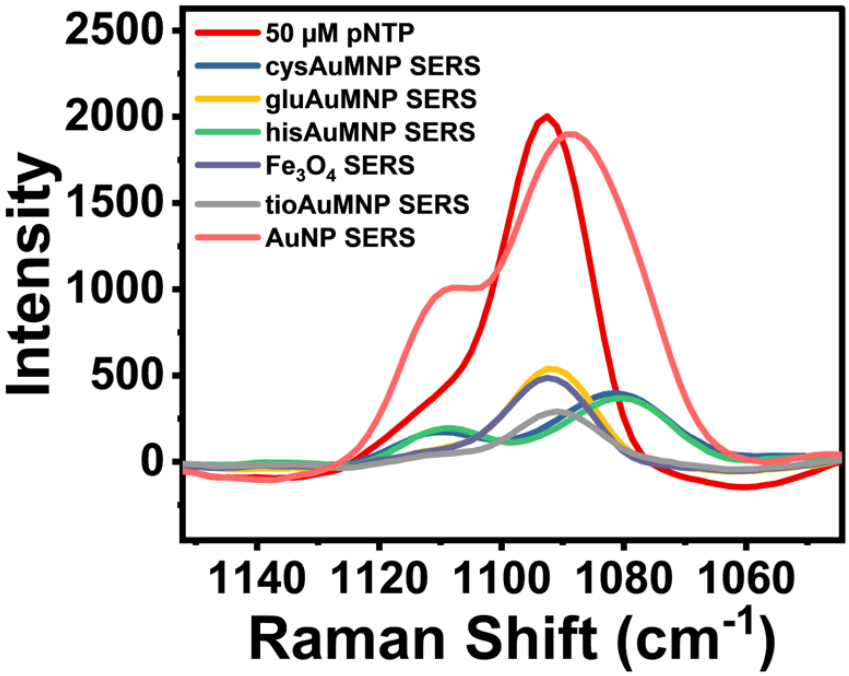

Fig. S16. Region of interest Raman/SERS spectrum over the 1080-1120 cm^{-1} band demonstrating the presence of a single peak in the dark red 50 µM *p*-NTP spectrum as opposed to splitting peaks in cysAuMNP, hisAuMNP, and the AuNP, as well as the tioAuMNP to some extent. The splitting phenomenon demonstrates the presence of a thiol-Au bond between the *p*-NTP and the Au nanoparticles.

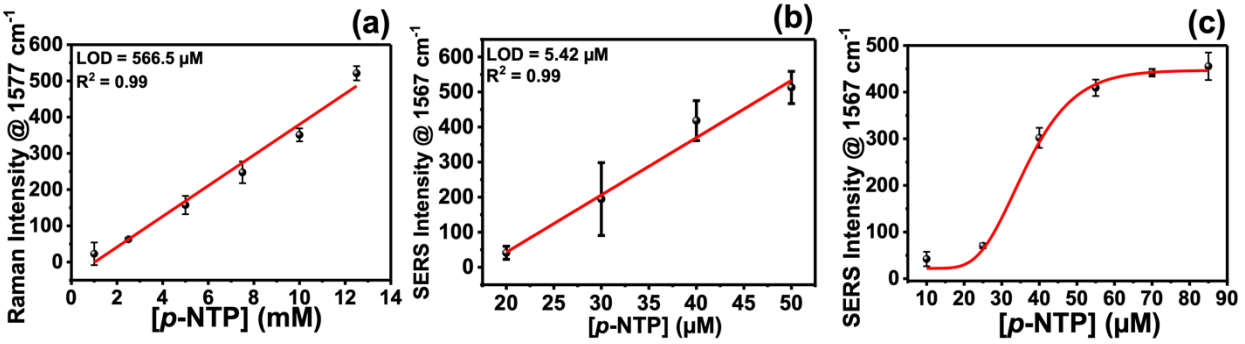

Fig. S17. Calibration curves for the Raman and SERS measurements on the portable Raman spectrometer. The limit of detection (LOD) was calculated using the 3σ method. The LOD for the natural Raman signal of the *p*-NTP (a) was 566.5 µM at the most intense peak (1577 cm^{-1}). The SERS LOD for *p*-NTP (b) when using cysAuMNP (nanoparticle with highest EF) was 5.42 µM, roughly 100x lower than the Raman LOD. The linear dynamic range (c) for this measurement is shown to be in the region of roughly 20-50 µM with qualitative detection still achievable above this region. All measurements were completed in triplicate.

Section 1. Calculation of SERS enhancement factor.

To quantify the enhancement factor of our nanoparticle in the liquid phase, we made multiple mathematical approximations to simplify the calculations. The general equation that was used for these calculations was

$$\text{(i)}\quad EF = \frac{N_{Raman} * I_{SERS}}{N_{SERS} * I_{Raman}}$$

where N_{Raman} is the number of molecules probed during natural Raman, I_{Raman} is the intensity of that natural Raman signal, N_{SERS} is the number of molecules probed during SERS, and I_{SERS} is the intensity of that SERS signal. The figure below demonstrates the first of these approximations, where in panel (**1**) the excitation scenario is demonstrated whereby the portable Raman's 785 nm excitation creates a roughly cylindrical excitation zone within the borosilicate vial. Therefore, we make a cylindrical approximation for this excitation zone (**2**) in order to simplify calculations and determine that given the spot size of the laser (25 µm) and the diameter of the vial (1 cm), the volume of excitation would be 4.91×10^{-12} m^3.

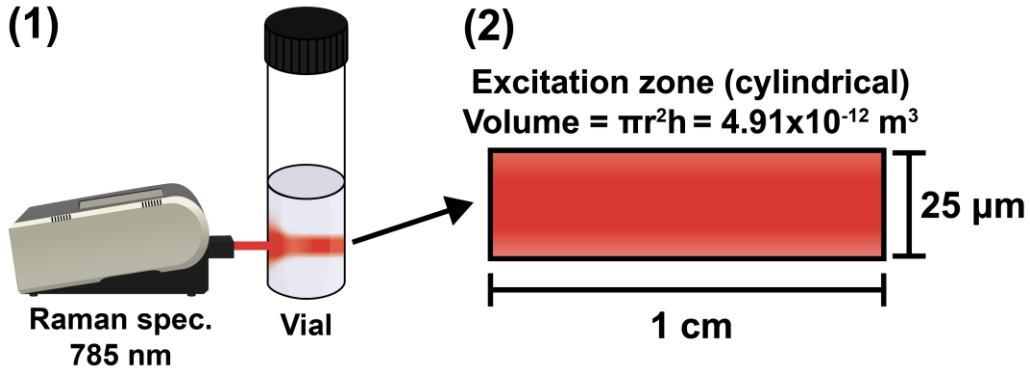

This value was then used to determine the number of molecules of both *p*-NTP and $AuFe_3O_4$ that would be located in this cylindrical excitation zone. To carry out this calculation, the following formula was used

$$\text{(ii)}\quad N_{\text{molecule}} = C_{\text{molecule}} * V_{cyl} * N_A$$

where $N_{molecule}$ was the number of *p*-NTP molecules in the cylindrical zone, $C_{molecule}$ was the concentration of *p*-NTP in solution (50 µM or 50 µmol/m^3), V_{cyl} was the volume of the cylindrical excitation zone (4.91×10^{-12} m^3), and N_A was Avogadro's constant (6.022×10^{23} mol^{-1}). From this equation one can see that the number of molecules of *p*-NTP in the cylindrical zone was $\underline{1.48 \times 10^8}$. This calculation in equation (**ii**) was carried out similarly for the $AuFe_3O_4$ nanoparticles where $C_{molecule}$ was 0.15 g/m^3, instead of 50 µmol/m^3 in the case of *p*-NTP. The value for $N_{molecule}$ in this case was found to be 4.44×10^{11} g•$AuFe_3O_4$/mol, with the unwanted units in the final value (units should not include g or mol) meaning that the molecular weight of the $AuFe_3O_4$ (g/mol) must be divided out of this number to obtain the number of molecules of $AuFe_3O_4$. Using the %Au loading for the $AuFe_3O_4$ obtained, cys$AuFe_3O_4$ has an Au:Fe ratio of 0.081:1, or 0.24 Au in 3 Fe, and

hisAuFe_3O_4 has an Au:Fe ratio of 0.360:1, or 1.08 Au in 3 Fe. This means that the molecular formula of cysAuFe_3O_4 would be essentially $Au_{0.24}Fe_3O_4$ (278.80 g/mol), and hisAuFe_3O_4 would have the formula $Au_{1.08}Fe_3O_4$ (444.26 g/mol). Factoring this into the number 4.44×10^{11} g•AuFe_3O_4/mol, we obtain 1.59×10^9 molecules of cysAuFe_3O_4 and 9.98×10^8 molecules of hisAuFe_3O_4. This is schematically represented below for clarity, where in panels (**3a**) and (**3b**) one can see the pictorial representations of this calculation in the cylindrical excitation zone.

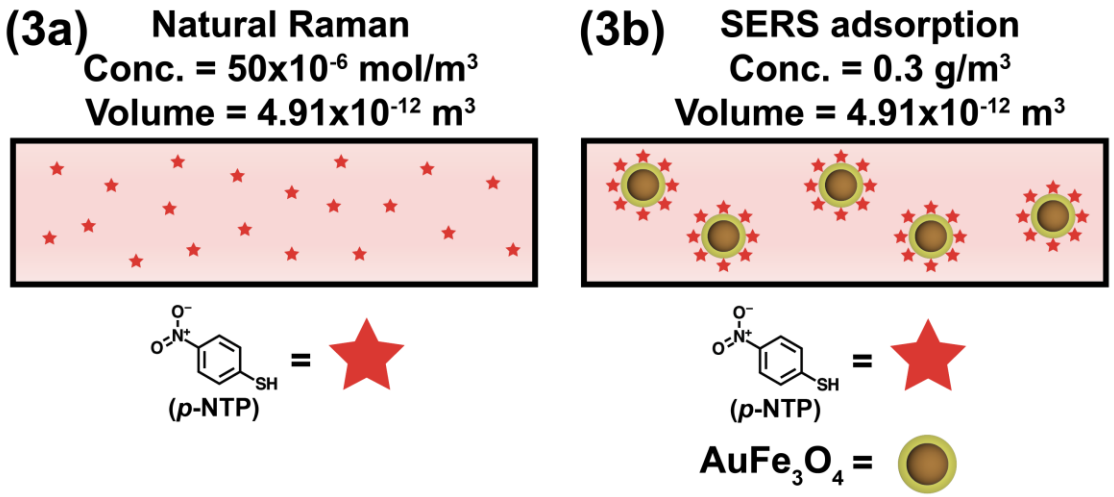

While from $N_{molecule}$ of *p*-NTP we immediately obtained the N_{Raman}, the N_{SERS} number has yet to be obtained as all that has been calculated was how many nanoparticles of AuFe_3O_4 are in the excitation zone. To identify the N_{SERS}, one must calculate the number of *p*-NTP molecules that would be contained in a SERS-active zone above the AuFe_3O_4.

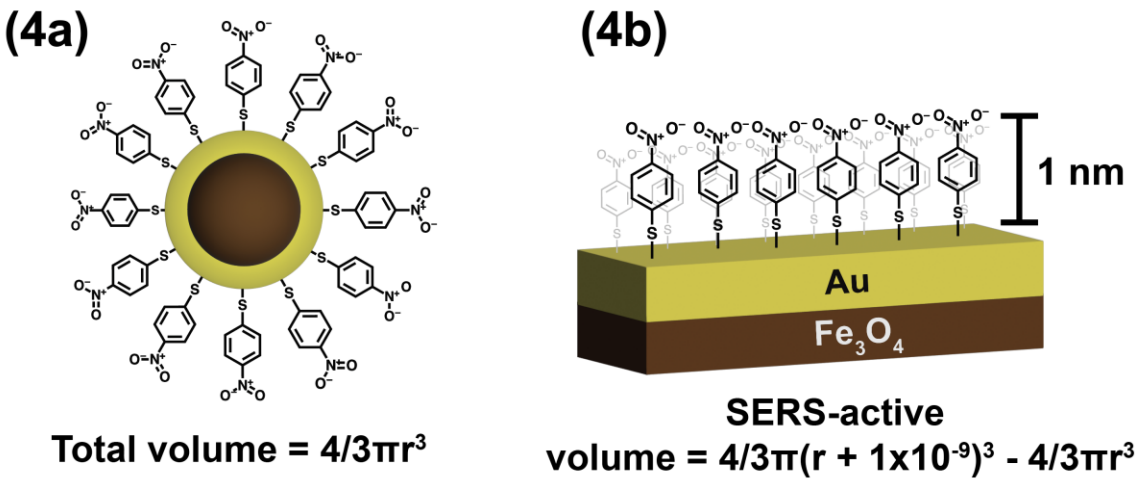

This is shown schematically above, where in panel (**4a**) one can see that if the entire volume of the nanoparticle was used the value would be $4/3\pi r^3$, however only a 1 nm surface above the nanoparticle is actually SERS-active (**4b**), therefore the formula for that volume is

$$\text{(iii) } V_{SERS} = \frac{4}{3}\pi(r + 1 \times 10^{-9})^3 - \frac{4}{3}\pi r^3$$

where *r* is the radius is the nanoparticle, with the first term ($r + 1x10^{-9}$) being the radius of the nanoparticle plus $1x10^{-9}$ m to account for a thickness of 1 nm above the surface. From the histograms obtained from STEM imaging, the *r* for cys$AuFe_3O_4$ is roughly 14.8 nm ($14.8x10^{-9}$ m), and the *r* for his$AuFe_3O_4$ is roughly 65.1 nm ($65.1x10^{-9}$ m). Therefore, for cys$AuFe_3O_4$ the V_{SERS} is $2.94x10^{-24}$ m^3, and for his$AuFe_3O_4$ is $5.41x10^{-23}$ m^3. This volume is then multiplied by the previous number of $AuFe_3O_4$ that would be found in this cylindrical zone ($1.59x10^9$ for cys$AuFe_3O_4$ and $9.98x10^8$ for his$AuFe_3O_4$) to determine the total SERS-active volume within the excitation zone. This was calculated to be a total volume of $4.67x10^{-15}$ m^3 for the cys$AuFe_3O_4$ and $5.40x10^{-14}$ m^3 for the his$AuFe_3O_4$. Substituting these volumes into equation (**ii**) in place of V_{cyl} allows us to obtain the N_{SERS} for both cys$AuFe_3O_4$ ($\underline{1.41x10^5}$) and his$AuFe_3O_4$ ($\underline{1.63x10^6}$). To complete the parameters needed for equation (**i**) in order to calculate SERS EF, we simply obtain I_{SERS} and I_{Raman} from the corresponding SERS and Raman spectra. The I_{SERS} was measured to be 259.5 counts for cys$AuFe_3O_4$ and 273.6 counts for his$AuFe_3O_4$, with the I_{Raman} being 46.1 counts for the 50 µM *p*-NTP. As previously stated, the N_{Raman} for 50 µM *p*-NTP was found to be $1.48x10^8$ and the N_{SERS} for cys$AuFe_3O_4$ and his$AuFe_3O_4$ were $1.41x10^5$ and $1.63x10^6$, respectively. Therefore, our SERS EF for cys$AuFe_3O_4$ was calculated as $\underline{5.91x10^3}$, and the SERS EF for his$AuFe_3O_4$ was calculated as $\underline{5.39x10^2}$.

Section 2. Optimized geometries and computational settings used for all four ligands.

1. Tiopronin, B3LYP/6-311G.

Atom	*Mass*	*x*	*y*	*z*
C	6.0	0.4703227643	0.1025178224	0.7495675075
C	6.0	1.5635511462	-0.6117405111	-0.0366550025
C	6.0	2.0886549628	0.2289648839	-1.1875263082
O	8.0	2.3126085012	1.4563557832	-1.0648369525
N	7.0	2.3055145629	-0.4246307161	-2.3616265716
C	6.0	2.8582325087	0.2676567888	-3.5135561251
C	6.0	2.9995830697	-0.7006754846	-4.6519440133
O	8.0	2.7142468000	-1.8989309776	-4.6070241697
O	8.0	3.4960483683	-0.0904518599	-5.7725766277
S	16.0	3.0562251667	-1.0812454064	1.0891315227
H	1.0	-0.4045486383	0.2705994540	0.1148525027
H	1.0	0.8236908670	1.0744909124	1.0905893675
H	1.0	0.1677475942	-0.4913424559	1.6102963630
H	1.0	1.2247130444	-1.5854378415	-0.3884872018
H	1.0	2.1594525955	-1.4191607168	-2.4545576619
H	1.0	3.8335604994	0.7057549803	-3.2838447246
H	1.0	2.2204059405	1.1011974610	-3.8169084454
H	1.0	3.5917976452	-0.7264886632	-6.5080287558
H	1.0	3.4179326013	0.2280365469	1.3544252968

2. Cysteamine neutral, B3LYP/6-311G.

Atom	*Mass*	*x*	*y*	*z*
C	6.0	-3.72402	2.20286	0.05682
C	6.0	-2.30854	1.63259	-0.05200
N	7.0	-4.73101	1.16316	-0.16946
H	1.0	-3.87667	3.00323	-0.67638
H	1.0	-3.88430	2.62731	1.05442
H	1.0	-4.67148	0.83356	-1.13273
H	1.0	-5.65942	1.57474	-0.07230
S	16.0	-1.06584	2.93790	0.18729
H	1.0	-2.14654	1.18298	-1.03737
H	1.0	-2.14620	0.85679	0.70370
H	1.0	0.00780	2.14003	0.09144

3. Cysteamine protonated, B3LYP/6-311G.

Atom	*Mass*	*x*	*y*	*z*
C	6.0	-10.0530859246	1.6209288182	0.0821942896
C	6.0	-8.7632596522	2.3979766812	0.3033128247
N	7.0	-11.2514316627	2.5587442327	0.0461528162
H	1.0	-10.2337955603	0.9116841118	0.8854349696
H	1.0	-10.0446845535	1.0858637976	-0.8630184582

S	16.0	-7.3307703447	1.1454071983	0.1054911725
H	1.0	-8.7100324564	2.8146632195	1.3046723802
H	1.0	-8.6201615874	3.1739558259	-0.4420641891
H	1.0	-6.3080872123	2.0398947338	0.3482985152
H	1.0	-11.3295821376	3.0863984751	0.9162869858
H	1.0	-12.1182098948	2.0383616093	-0.0866527711
H	1.0	-11.1803590133	3.2366512964	-0.7147085355

4. Glutathione, B3LYP/6-311G.

Atom	*Mass*	*x*	*y*	*z*
C	6.0	1.0510336730	0.1064383750	0.4407194051
C	6.0	0.4261909856	-1.2375095199	0.8285182428
C	6.0	-1.0900341592	-1.1668536101	0.8665592560
O	8.0	-1.7436542895	-0.3599932648	0.1647025913
N	7.0	-1.7031143709	-2.0700345407	1.6909700734
C	6.0	-3.1511685549	-2.1646894617	1.8127951953
C	6.0	-3.7330527121	-3.4210642831	1.1360798852
S	16.0	-3.4326382497	-3.3677340676	-0.7497299283
C	6.0	-3.4882918269	-2.2321939680	3.3065549083
O	8.0	-2.7496058971	-2.8537185680	4.1080412572
N	7.0	-4.6347989543	-1.6257544476	3.7041973398
C	6.0	-5.0768933083	-1.6924596183	5.0867962136
C	6.0	-6.4688277544	-1.1054773364	5.1940427807
O	8.0	-7.0729830135	-0.6107594037	4.2514721943
O	8.0	-7.0412372882	-1.1410770176	6.4448337831
C	6.0	2.5666756388	-0.0148389917	0.1566718189
C	6.0	3.1276273013	1.3307510034	-0.3308976529
O	8.0	3.9787739381	1.9800433890	0.2619396432
O	8.0	2.6149636745	1.8125926189	-1.5270970461
N	7.0	3.2733469050	-0.5256321862	1.3270620940
H	1.0	0.5151221656	0.4980672317	-0.4263221227
H	1.0	0.8992809959	0.8361490070	1.2420725187
H	1.0	0.8401590656	-1.5817717529	1.7760467367
H	1.0	0.6950751959	-1.9969933315	0.0841598488
H	1.0	-1.1658695884	-2.6360213412	2.3316127884
H	1.0	-3.5715750080	-1.2691252726	1.3538416337
H	1.0	-4.8072556356	-3.4717227562	1.3026594385
H	1.0	-3.2535174580	-4.3111759503	1.5367938423
H	1.0	-3.9186563154	-4.6439527034	-0.9825380914
H	1.0	-5.2215901071	-1.1025667674	3.0685237663
H	1.0	-4.3933397565	-1.1428656811	5.7438642224
H	1.0	-5.0686131829	-2.7303674925	5.4330708174
H	1.0	-6.4877557219	-1.5574799588	7.1314446398
H	1.0	2.7022127154	-0.7374864297	-0.6562196019
H	1.0	1.9215533203	1.2459644485	-1.9115216693
H	1.0	3.3447699116	0.1669009288	2.0650816728
H	1.0	4.1936776661	-0.8904672791	1.1136075044

5. Histidine, B3LYP/6-311G.

Atom	*Mass*	*x*	*y*	*z*
C	6.0	-1.9381642864	-1.5077724201	-0.7364225444
C	6.0	-1.5738211505	-0.2251609807	-0.3677065973
N	7.0	-0.3235089906	-0.3743357426	0.2346511499
C	6.0	0.0150247281	-1.7021963638	0.2032103451
N	7.0	-0.9434132742	-2.4236601053	-0.3788044555
C	6.0	-2.2465723556	1.1022446162	-0.5293891563
C	6.0	-2.9905470237	1.6592970263	0.7508965253
C	6.0	-4.3216806899	0.9467919531	0.9337113873
O	8.0	-5.4238094164	1.4867579770	0.8387586542
O	8.0	-4.2731809366	-0.4038232201	1.1929985574
N	7.0	-3.2298690627	3.0956424133	0.7288460035
H	1.0	-2.8260893187	-1.8228052804	-1.2544941380
H	1.0	0.2439851224	0.3633849566	0.6182266593
H	1.0	0.9372814534	-2.0818284096	0.6029756875
H	1.0	-2.9576609587	1.0515723033	-1.3555592536
H	1.0	-1.5075920438	1.8582872588	-0.8013078640
H	1.0	-2.3683375815	1.4289907945	1.6201604386
H	1.0	-3.3752509413	-0.7945435805	1.1711559573
H	1.0	-3.9537390225	3.3814690224	0.0815533360
H	1.0	-2.3868642508	3.6445477817	0.6244293076

References

[1] M. Stoia, R. Istratie, and C. Păcurariu, "Investigation of magnetite nanoparticles stability in air by thermal analysis and FTIR spectroscopy," *Journal of Thermal Analysis and Calorimetry*, vol. 125, no. 3, pp. 1185-1198, 2016/09/01, 2016.

[2] M. Zarghani, and B. Akhlaghinia, "Fe3O4 magnetic nanoparticles (MNPs) as an efficient catalyst for selective oxidation of benzylic and allylic C–H bonds to carbonyl compounds with tert-butyl hydroperoxide," *RSC Advances*, vol. 6, no. 45, pp. 38592-38601, 2016.